Solution of Nonlinear Finite Difference Ocean Models by Optimization Methods with Sensitivity and Observational Strategy Analysis

JENS SCHRÖTER

Max-Planck Institut für Meteorologie, 2000 Hamburg 13, FRG

CARL WUNSCH

Center for Meteorology and Physical Oceanography, Department of Earth, Atmospheric and Planetary Sciences, Massachusetts Institute of Technology, Cambridge, MA 02139

(Manuscript received 5 December 1985, in final form 6 May 1986)

ABSTRACT

Dynamical models driven by "observed" forcing fields (e.g., the wind) have a true solution uncertainty owing to observational errors in the driving. This uncertainty is usually hidden from view because conventional numerical methods do not easily calculate it. We explore with finite difference, nonlinear circulation models (one and two layer) the uncertainties in interesting flow properties, such as western boundary current transport, potential and kinetic energy, owing to the uncertainty in the driving surface boundary condition. The procedure is based upon nonlinear optimization methods. The same calculations permit quantitative study of the importance of new information as a function of type, region of measurement and accuracy, providing a method to study various observing strategies.

Uncertainty in a model parameter, the bottom friction coefficient, is studied in conjunction with uncertain measurements. The model is free to adjust the bottom friction coefficient such that an objective function is minimized while fitting a set of data to within prescribed bounds. The relative importance of the accuracy of the knowledge about the friction coefficient with respect to various kinds of observations is then quantified, and the possible range of the friction coefficients is calculated.

1. Introduction

When modeling the general circulation of the ocean, one is confronted with, among others, two major problems. First, the models used are never exact. To reduce the number of degrees of freedom (formally infinite in number), approximations are made to the Navier-Stokes equations, sometimes by complete elimination of some physics, or by crude parameterizations using empirical coefficients of uncertain value.

The second problem is that the measured data available to determine model parameters, or to set the boundary conditions, are never wholly adequate. Apart from the notorious problems of inadequate coverage of large oceanic areas, all data contain noise from instrumental and other errors.

Both these problems introduce uncertainties into descriptions of the ocean circulation. Unfortunately, for the complex numerical models required to describe the ocean, the methods used to find solutions do not lend themselves to determining the degree of uncertainty of the model solutions, an uncertainty which will normally be a very complex function of model, position, time and data type. The absence of this information about uncertainty in turn makes it difficult to study experimental design—for example, to ask what the impact would be on existing uncertainties of different types of new observations with differing error budgets?

In this present paper we explore the solution of conventional finite difference models by methods designed specifically to determine the solution uncertainties and to permit (reasonably) easy exploration of observational strategies. Our immediate purpose is not to present particularly realistic examples; rather it is to explore a general class of model, and a class of numerical methods, whose application in this context seems novel. This present paper is intended to be a stage in a learning process toward an ultimate capability for using the most sophisticated of baroclinic EGCMs (a process already underway in Hamburg). A preliminary description of this work was given by Schröter (1984); a related study, involving a linear finite difference advection/diffusion model was published by Wunsch (1985). Among the models used here are some that are nonlinear and also baroclinic. In terms of the most general models one expects eventually to use, the greatest limitation is in the assumption of steady flow. But as we will discuss at the end, the introduction of the time variable can be regarded as a conceptually straightforward extension

of the methods employed here; the major issues are those of available computer power, rather than of any change in principle.

Our numerical procedures are probably best referred to as "optimization methods". But they have much in common with (and to a large extent are indistinguishable from) other methods called variously objective mapping, assimilation, inverse methods, mathematical programming, optimal control, etc. In particular, when the models are run in the nonlinear parameter range, we are performing a nonlinear inverse procedure. We would distinguish our procedures from assimilation methods, which are highly developed in meteorology, in two ways: we put a major emphasis on understanding which model parameters and fields are actually determined and how well, and by which of the observations; and (in other contexts where time variation is included) we put little or no emphasis upon the forecast problem. We believe that for most oceanographic problems for the indefinite future, the emphasis will be on determining and understanding the state of the ocean at some particular time rather than predicting its future state (an obvious exception is the El Niño problem). In this way, observations taken over a span of time will be combined together to make an optimum estimate of the ocean even when some of them are formally "future" to the specific time under consideration.

The present paper and the independent study of Malanotte-Rizzoli and Holland (1986) also provide a contrast. Their approach is more akin to the meteorological practice of direct insertion of observations into the model, with the subsequent solution found by conventional methods. Our own emphasis is on understanding how to deal with uncertainty and has led us to emphasize a different approach to the solution.

The purpose of the work of Sasaki (1958), Wahba and Wendelberger (1980) and of Bennett and McIntosh (1982) is philosophically close to what we are doing. In those studies, uncertain, often sparse measurements are best-fit to a set of kinematical and dynamical constraints using a variational principle. Although the goals and philosophy of these other efforts are very similar to ours, the procedures are quite different. The differences in our approach are probably best appreciated after the problem is formulated and solved.

We study first the problem of "inadequate" input data for finite difference ocean models. Inadequate in this context means unequally distributed, with gaps and points, or regions of poor accuracy or both. The attribution of the data to the gridpoints of models is traditionally done by interpolation, filtering, objective mapping, etc., which leads to uneven accuracy at individual grid points. But finite difference ocean models do not normally distinguish between more or less reliable input data. Here we write the model equations that involve measured data as inequalities instead of equalities, as a reflection of the inevitably varying accuracy of the data. The resulting system can no longer be solved uniquely; only a "best" solution can be found. "Best" in this context means a solution that optimizes an objective, characteristic quantity while the inequalities act as constraints. This "objective function" depends on the question one is trying to answer; e.g., "what is the maximum (minimum) flow through a strait that is compatible with the measured data and with their respective accuracy?". Apart from putting bounds on the solution one can also seek the most probable solution. In this paper we concentrate on the bounds. If upper and lower bounds are close together, we might be satisfied with the result and disregard the indeterminacy that remains in the details of the solution (see the discussion in Wunsch, 1984).

It is a major advantage of the method we use that we can calculate the change of the extreme value of our objective function when the value of any of the measured data is changed or, even more important, when additional data are introduced.

More generally, a large number of questions can be answered following this approach:

- What is the set of possible solutions, S, to a problem with a given set of measured input data, and which is the most probable solution? Is the dataset contradictory and what can we learn if this appears to be the case?
- Does the inclusion of an additional dataset (perhaps of a completely different kind), reduce S and to what extent? Is the new information compatible with the previous information?
- Where and how accurately would we have to make new measurements if we want to reduce S; what are the regions where we do not have to measure at all?
- To what extent does the a priori knowledge about the input data, such as estimated extrema, shape of the spectrum, etc., make the actual measurement of the data unnecessary?
- What is the quantitative sensitivity of the value of our objective function to measurements of different kinds and in different regions?
- Is it more important to obtain better measurements or to improve parameterizations in the model such as eddy diffusivity coefficients, or the description of the bottom topography?

Note that the objective function will often describe directly the question we are interested in.

2. The single layer model

For this study we have chosen the model of the wind-driven circulation in a square basin of uniform depth D and sides L on a β-plane used by Veronis (1966a,b), and Harrison and Stalos (1982).

The nondimensional differential equation that describes the circulation is the time independent, vertically integrated vorticity equation.

$$RJ(\Psi', \nabla^2\Psi') + \frac{\partial \Psi'}{\partial x'} + \epsilon \nabla^2 \Psi' - \text{curl}\tau' = 0 \qquad (1)$$

where Ψ' is the transport streamfunction. Transports are $u' = -\partial\Psi'/\partial y'$ and $v' = \partial\Psi'/\partial x'$, τ' is the surface windstress, and J denotes the Jacobian operator. Boundary conditions for (1) are $\Psi' = 0$ at $x' = 0, \pi$ and $y' = 0, \pi$. Equation (1) was made nondimensional by defining

$$x' = \frac{x}{L}\pi, \quad y' = \frac{y}{L}\pi, \quad \Psi' = \Psi \frac{D\beta}{A} \qquad (2)$$

where A is the maximum absolute value of $\text{curl}\tau$. Nondimensional quantities are temporarily denoted by primes. The friction parameter is

$$\epsilon = \frac{K\pi}{\beta L} \qquad (3)$$

and the Rossby number,

$$R = \frac{A\pi^3}{D\beta^2 L^3} \qquad (4)$$

where K is a coefficient of bottom friction. The nondimensional forcing is

$$\text{curl}\tau' = -\sin x' \sin y' \qquad (5)$$

The primes will be dropped hereafter.

The differential equation (1) is transformed into a finite difference equation by approximating the derivatives as centered differences (Roache, 1982). The Jacobian is approximated in such a way that $\nabla^2\Psi$ need not be specified at the boundaries; thus no one-sided approximations of $\nabla^2\Psi$ are necessary (Veronis, 1966b).

The solution $\hat{\Psi}$ of (1) has strong gradients near the western and northern boundaries. To describe them adequately, we have chosen a mesh that is stretched proportional to $\sin^2(x/2)$ and $\sin^2(y/2)$ with best resolution at the boundaries.

Here ϵ was set to 0.05, the value that Veronis (1966a,b) and Harrison and Stalos (1982) studied most intensively during their computations. For small R, ϵ describes the width of the western boundary current. Because of the grid-stretching, 13 points are sufficient in either coordinate to describe the solution. The finite difference representation of (1) with (5) is thus a collection of 13×13 nonlinear algebraic equations which we denote

$$\mathbf{M}(\Psi) = \mathbf{0}. \qquad (6)$$

The functional $\mathbf{M}(\Psi)$ and the vector of unknowns Ψ each have 169 components. The linear problem ($R = 0$) was solved by Stommel (1948). We solved the same problem using the optimization technique described below. Our numerical solution of (6) compares favourably with the analytical solution (Fig. 1). In this figure the streamfunction has been normalized by its maximum value $\Psi_{\max}$ and the contour interval was set to 0.2 (the same normalization applies to all subsequent contour plots in this paper).

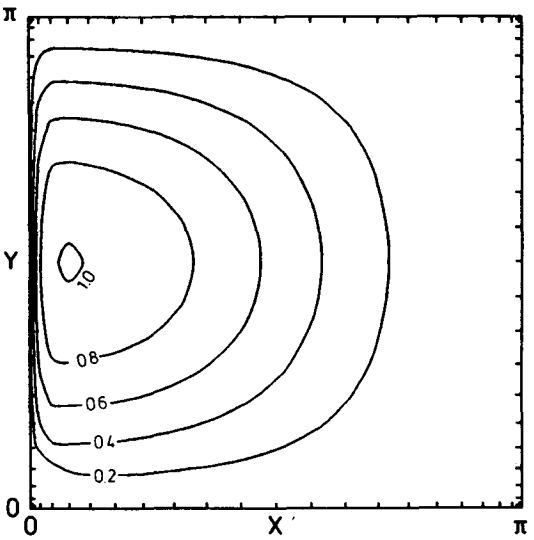

FIG. 1. Normalized streamfunction $\Psi/\Psi_{\max}$ for the Stommel-problem. Parameters are $\epsilon = 0.05$, $R = 0.0$. $\Psi_{\max} = 1.85$.

In the nonlinear regime we put $R = 0.01$. This value gives rise to a small northern boundary current that does not quite reach the eastern boundary. The width of the boundary currents is increased to $\sqrt{R}$ as inertial effects dominate. A small recirculation zone is observed (see Fig. 2). These two solutions for the linear and the nonlinear problem ($R = 0$ and $R = 0.01$) will be regarded as the "true" or "fully posed" solution of the model because in these cases there is no uncertainty in the forcing $\text{curl}\tau$, nor in any model parameters.

3. Model modifications and solutions

a. Uncertainties in the forcing field

In a realistic situation, there will be some uncertainty in $\text{curl}\tau$ and we let it deviate slightly from its "true" value $-\sin(x)\sin(y)$. At each gridpoint j, a lower and an upper limit for the deviation is

$$L_j \leqslant (-\sin(x)\sin(y) - \text{curl}\tau)_j \leqslant U_j, \quad j = 1, \cdots, 169. \qquad (7)$$

We can no longer ask for a solution that fulfills (6) exactly. Consequently Eqs. (6) are then rewritten as a set of range inequalities, or in vector form as

$$\mathbf{L} \leqslant \mathbf{M}(\Psi) \leqslant \mathbf{U}. \qquad (8)$$

Each equation $M_j(\Psi) = 0$, $j = 1, \cdots, 169$ of (6) is permitted to be violated by an amount that is within the bounds of Eq. (8). Upper and lower bounds in (8) need not be the same. An advantage of the formulation (8) is that the uncertainty in the forcing would normally be position dependent. Note that there exists an exact

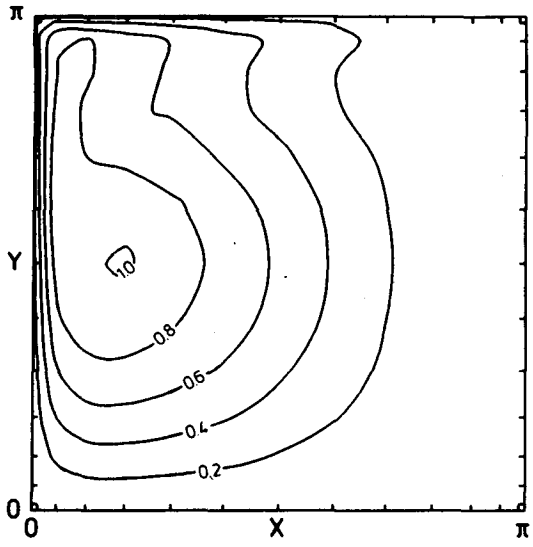

FIG. 2. As in Fig. 1 but for the nonlinear problem, $R = 0.01$. $\Psi_{max} = 1.80$.

solution $\hat{\Psi}$ of the original Eq. (1) for every forcing field curl_τ obeying (7).

Only in the case of $\mathbf{L} = \mathbf{U} = \mathbf{0}$ is the solution unique. Then the problem is fully posed and we obtain the "true" solution of Figs. 1, 2. In all other cases there is an infinite number of solutions for (8). For many purposes we are not interested in a solution $\hat{\Psi}$ itself but rather in some of its properties. Consequently we will not describe the set of solutions of (8) directly, but will seek information about its properties (i.e., find bounds for them). Interesting properties of the circulation that can be modeled with a nonlinear barotropic model are western boundary current transports, potential or kinetic energies, etc. To tackle other questions, such as meridional heat transport, a more complicated ocean model has to be used (see section 5).

We define a number of diagnostic objective functions, $F_i(\Psi)$, that describe interesting features of the flow. The following ones have been used.

(i) $F_1 = \Psi_{max}$:

F_1 is to be interpreted as the western boundary current transport and is linear in Ψ.

(ii) $F_2 = \int \Psi^2 da$:

$F_2 \propto$ potential energy and is nonlinear in Ψ; da is the area differential.

(iii) $F_3 = \int (\nabla\Psi)^2 da$:

$F_3 \propto$ kinetic energy and is nonlinear in Ψ.

We will look for solutions that drive one of the quantities F_i to its extreme minimum or maximum value. That is, we will solve the problem:

$$\text{Minimize } F(\Psi) \quad \text{subject to} \quad \mathbf{L} \leqslant \mathbf{M}(\Psi) \leqslant \mathbf{U}. \tag{9}$$

$F(\Psi)$ is any one of the F_i. For maximization, we replace $F(\Psi)$ by $-F(\Psi)$ in (9).

b. *Numerical procedures*

The minimizing of the objective function subject to the range constraints is made by an iterative algorithm with the use of a sequential augmented Lagrangian method (Gill and Murray, 1972; Luenberger, 1984).

First, the range inequalities (9) are converted into equalities by adding bounded slack variables Y_j to them.

$$M_j(\Psi) + Y_j = 0 \quad \text{subject to}$$
$$L_j \leqslant -Y_j \leqslant U_j \quad j = 1, \cdots, m. \tag{10}$$

A new vector $\mathbf{X}$ of unknowns is defined. The first n components are the previous unknowns Ψ_i, $i = 1, \cdots, n$ (with $n = 169$ here). The next $m = 169$ components are the slack variables Y_j corresponding to the constraints.

By introducing the slack variables, the total number of variables is increased from n to $n + m$. The new equality constraints are written

$$\mathbf{C}(\mathbf{X}) = \mathbf{0} \quad \text{subject to} \quad L_j \leqslant -X_{n+j} \leqslant U_j \quad j = 1, \cdots, m \tag{11}$$

where $\mathbf{C}$ is an m functional and $\mathbf{X}$ the $n + m$ vector of unknowns. Thus we have changed the $2m$ inequalities (9) with n unknowns to m equalities (11) with $n + m$ unknowns. The set of $\mathbf{X}$ for which (11) holds is denoted as the set of "feasible" solutions—in the jargon of linear and nonlinear programming. Although the Eq. (6) are no longer exactly satisfied, the solution does exactly satisfy the original dynamical model (1), albeit the forcing function, curl_τ, now differs from the value initially estimated. Thus the nature of the solution and its relationship to the underlying hypothetical solution to the original continuous partial differential equation can be inferred from known properties of the finite difference scheme. A referee has raised the question of whether the finite difference methods we (and our predecessors) use will yield uniformly valid solutions to the underlying partial differential equation. Such a discussion is beyond the scope of the present paper in which for our purposes, the ocean model may be viewed as the finite difference analogue equation, rather than the continuous version.

c. *Inserting additional data*

To test the usefulness of other types of information than the dynamics of the flow described by the model (1) and the forcing field with its prescribed uncertainty, we will insert additional data into the model. This can be done either to further constrain the flow with existing data or to study the question "how accurate would I have to make future measurements in order to gain new information that is not already included in (11)?"

We will investigate with our single layer model two different kinds of additional measurements. The first type simulates satellite altimetry, and the second simulates acoustic tomography.

In the barotropic model, the sea surface topography and the transport streamfunction are equivalent. Consequently, altimetric measurements are simulated by taking the streamfunction from the fully posed solution and multiplying it by a scaling factor, γ, chosen such that the maximum of the streamfunction corresponds to a one-meter sea surface elevation. The absolute measurement error for the surface elevation including geoid error is $\pm\Delta Z$. The topographic constraints for the model are

$$-\Delta Z \leqslant (\Psi - \Psi_{\text{fully posed}})\gamma \leqslant \Delta Z, \tag{12}$$

where both streamfunctions are taken along the satellite "track". Consider a track that runs from west to east along y = constant. As this track covers 13 gridpoints, Eq. (12) describes 26 inequalities. They are changed to 13 equalities by adding bounded slack variables. The new equalities are added as additional elements to $\mathbf{C}(\mathbf{X})$. We obtain (formally) the same expression as before

$$\mathbf{C}(\mathbf{X}) = \mathbf{0} \quad \text{subject to} \quad L_j \leqslant -X_{n+j} \leqslant U_j \quad j = 1, \cdots, m.$$

The dimensions of $\mathbf{C}$, $\mathbf{X}$, $\mathbf{L}$ and $\mathbf{U}$ have all been increased by 13, i.e., $m = 182$. (All constraints in this paper are defined in such a way that the upper bound corresponds to a stronger, and the lower bound, to a weaker flow.)

The second simulated measurement to be tested for its usefulness relative to previous data is derived from acoustic tomography. Let b be an area inside the ocean basin that is surrounded by an array of acoustic transceivers. As discussed by Munk and Wunsch (1982), by measuring the difference in travel time between the clockwise and the anticlockwise sound paths, a very accurate value for the integral of the velocity along the circumference of the area b is obtained as

$$\Gamma = \int \mathbf{v} \cdot d\mathbf{s} = \int \nabla^2 \Psi \, db. \tag{13}$$

We suppose here that the circulation is determined around a number of areas, b, that fill the interior of the basin. Choose b_j to consist of an area represented by nine adjacent gridpoints. If we omit all gridpoints that are next to a boundary where the vorticity $\nabla^2\Psi$ might become very large, we can define up to 81 (overlapping) areas b_j. The "measured" data are again obtained from the fully posed solution and the actual circulation permitted to deviate from these data to within some bounds.

$$L_j \leqslant \Gamma_j - \Gamma_{j,\,\text{fully posed}} \leqslant U_j \quad j = 183, \cdots, 246. \tag{14}$$

By the addition of slack variables to (14) we derive again problem (11), where now the dimension is increased to 263.

Many other types of observations can be handled in this way, but we will refrain from displaying further examples.

d. The minimizing routine

We turn now to some of the numerical details. In all cases, the formal problem is

$$\text{Min } F(\mathbf{X}), \quad \text{subject to} \quad \mathbf{C}(\mathbf{X}) = 0,$$
$$L_j \leqslant -X_{n+j} \leqslant U_j, \quad j = 1, \cdots, m. \tag{15}$$

Following Luenberger (1984), we construct the augmented Lagrangian function $L(\mathbf{X}, \lambda, \delta)$,

$$L(\mathbf{X}, \lambda, \delta) = F(\mathbf{X}) + \lambda^{\mathrm{T}}\mathbf{C}(\mathbf{X}) + \delta\mathbf{C}(\mathbf{X})^{\mathrm{T}}\mathbf{C}(\mathbf{X}). \tag{16}$$

The δ and λ are a positive penalty parameter and the m-vector of the appropriate Lagrange multipliers respectively; T denotes the vector transpose.

Here $F(\mathbf{X})$ is the previously defined objective function. The slack variables X_{n+j}, $j = 1, \cdots, m$, in (16) do not contribute to F. An initial penalty parameter δ_0 and an initial vector of variables $\mathbf{X}_0$ have to be provided; $\mathbf{X}_0$ need not be "feasible".

For a sufficiently large δ, the function L is convex, provided $F(\mathbf{X})$ is convex, and an unconstrained iterative minimization technique can be applied. A so-called quasi-Newton method is used to find a direction of descent for L, and a line search is carried out along this direction. Either a minimum is found during this search, or one of the simple bounds on $\mathbf{X}$ is encountered. From this point, a new direction is calculated, etc., until the convergence criteria which are defined in the next section are fulfilled. During the computation it may turn out that the initially chosen δ was too small and the algorithm has reached an $\mathbf{X}$ where the Hessian of L with respect to those components of $\mathbf{X}$ that are not at their bounds is not positive definite (i.e., L is not locally convex). In this case δ is augmented, and the whole sequence of calculations is started again from the current point.

To reduce the amount of work required within the iterations, an "active set" strategy is adopted: certain variables (original or slack variables) that are at their bounds at a given iterate are considered "active". The search direction is chosen so that the same variables are also active at the next iterate. This reduces the degrees of freedom of the problem, as we can do the minimization in the lower dimensional subspace that is spanned by the remaining variables (denoted "free" variables). During the line search, one of the free variables may encounter a bound or one of the active variables on a bound may become a free variable. The set of free variables is thus altered as the minimization proceeds, until eventually the correct set of the free variables is identified.

This algorithm was chosen because it combines the advantages of the Lagrange multiplier method and the

penalty function method for constrained minimization, while eliminating many of the disadvantages associated with either method alone (Luenberger, 1984). Because it is not necessary for δ to go to infinity to enforce the equality constraints $\mathbf{C}(\mathbf{X}) = \mathbf{0}$, the ill-conditioning of the Hessian of L usually associated with the penalty function approach is ameliorated. Indeed it is not necessary for δ to be large in order to let L attain its minimum at a "feasible" point. On the other hand, it is no longer necessary to provide that $\mathbf{C}(\mathbf{X}) = \mathbf{0}$ during the process of the minimization, and an unconstrained procedure can be applied. We use a subroutine from the Numerical Algorithms Group (1984).

If the objective function $F(\mathbf{X})$ is not convex, i.e. it has more than one local minimum, we can find the global minimum only by starting the algorithms from different initial $\mathbf{X}_0$ and, if necessary, provide an upper bound for changes in $\mathbf{X}$ during the iterations. When $F(\mathbf{X})$ is convex, as it is for all the nonlinear forms we have used, and as it normally is for the linear one as well, then the solution Ψ which leads to the optimum value of F is unique. This behavior contrasts with that of the linear programming problem of Wunsch (1984).

e. *Convergence criteria*

As we use an iterative procedure, a sequence of $\mathbf{X}_k$ is generated that converges to the optimal solution $\hat{\mathbf{X}}$. At some iteration step k, changes in the current solution $\mathbf{X}_k$ and consequently changes in the value of the objective function $F(\mathbf{X}_k)$, and the values of the constraints $\mathbf{C}(\mathbf{X}_k)$, become negligible and further iterations are meaningless. In order to reduce the computation time we have defined "negligible" rather loosely. We allow the constraints to be violated by small amounts, i.e. the rms violation (denoted "$\mathbf{C}_r$" hereafter) is smaller than 10^{-6}. As this translates into accuracies for the objective function and the unknowns $\mathbf{X}$ of at least 5 significant digits, we are prepared to accept this small infeasibility of the solution. By performing more iterations, we could make $\mathbf{C}_r$ arbitrarily small without any significant change in $\hat{\mathbf{X}}$.

A second convergence criterion is that the derivatives $\partial F(\mathbf{X})/\partial X_i$ are zero for those variables X_i that are not at their upper or lower bounds, i.e. that a stationary point is reached. A further criterion ensures that the Lagrange multipliers λ are calculated to an accuracy of at least three significant digits and that all nonzero multipliers are encountered.

f. *Scaling*

It is important to scale the constraints appropriately. Scaling does not change the solution $\hat{\mathbf{X}}$, but significantly influences the convergence toward the solution. To find the proper weight to be applied to a constraint C_j we have to find a compromise between two requirements. To make the Hessian of $L(\mathbf{X}, \lambda, \delta)$ well conditioned, C_j should be multiplied by a weight W_j such that, ideally, the derivatives $\partial C_j/\partial X_i$ that are not zero are close to one. Note that independent of W_j, the derivative of C_j with respect to the slack-variables X_{n+i} is δ_{ji}. The other goal is to choose W_j such that the Lagrange multipliers λ_j are of approximately equal magnitude. At the solution $\hat{\mathbf{X}}$, the λ_j are the derivatives of the objective function F with respect to marginal changes in the bounds of the constraint C_j, i.e., to the bounds of the slack variable X_{n+j}. The λ_j are thus inversely proportional to W_j. Other scaling requirements are that at the solution $\hat{\mathbf{X}}$:

- The components of $\mathbf{X}$ should be of equal size, preferably between 0 and 1.
- The value of the objective function $F(\mathbf{X})$, should be close to 1.
- The derivatives $\partial F/\partial X_i$ should be close to 1.

All these requirements are made to reduce the importance of rounding errors and loss of significant digits during the iterative process.

For the current problem, we have found that the scaling of the objective function $F(\mathbf{X})$ and of the unknowns $\mathbf{X}$ was sufficient, once the vorticity equation had been made nondimensional.

g. *The Lagrange multipliers: Interpretation*

The Lagrange multipliers appearing in (16) play a very important role in what follows. Luenberger (1984) has a clear account of the role and meaning of the Lagrange multipliers; we limit ourselves to a brief summary sufficient to interpret our results. When $\mathbf{X} = \hat{\mathbf{X}}$ is substituted into (15), this solution satisfies all the equality constraints and all the inequality constraints. Because the solution is an optimizing one, many of the inequality constraints will lie at the very upper or lower limits of their range; such limiting inequalities are said to be "active" or "binding". Equality constraints are always binding. It is intuitively clear that perturbations to the bounds of the nonbinding constraints leave the solution, and hence the value of the objective function, unchanged. On the other hand, perturbations in the rhs values of binding constraints necessarily change the solution and hence the objective function. It may be shown without difficulty (Luenberger, 1984) that the Lagrange multipliers of the problem represent the *sensitivity* of the objective function to the rhs perturbations:

$$\lambda_j = -\frac{\partial F}{\partial U_j}, \lambda'_j = -\frac{\partial F}{\partial L'_j}$$

or in vector form

$$\lambda = -\partial F/\partial \mathbf{B},$$

where $\mathbf{B}$ is the vector of upper and lower bounds. The Lagrange multiplier for any nonbinding or inactive constraint is necessarily zero, corresponding to the lack

of influence. The convention is that positive λ_i indicates that the corresponding constraint has reached its upper bound, while a negative λ_i shows that the lower bound has been encountered. *By making maps of the Lagrange multipliers of our problem we can thus easily and conveniently display those constraints (observational or dynamical) to which our particular answer is most sensitive and so determine which are most important.* The relationship to the problem of designing observational strategies will be obvious. In linear programming, a special case of the present method, the Lagrange multipliers are usually labeled the "dual" solution.

The forcing constraints $C_j, j = 1, \cdots, 169$ describe a finite difference approximation of a differential equation calculated at a grid point, which, in turn, is representative for a small area a_j. Because a stretched grid was used, these areas are unequal. To compensate for the unequal importance of the constraints, they have been weighted by their corresponding area a_j. The corresponding Lagrange multipliers λ_j are then independent of the grid-stretching, and *describe the sensitivity of the objective function F with respect to changes in the forcing per unit area.* Tomographic, altimetric and circulation constraints are weighted in the same way by their appropriate areas a_j and b_j, respectively.

Further comments on practical experience with the computational algorithm may be found in the Appendix.

4. Sensitivity analysis

The optimization technique was applied to a variety of problems. By including different constraints with appropriate bounds for their respective uncertainties, we have explored the relative usefulness of different kinds of data.

a. No uncertainty in the forcing

Let us first consider the case where $\mathbf{L} = \mathbf{U} = \mathbf{0}$ and none of the auxiliary "data" are used. That is, we are solving the conventional, fully posed numerical model of equations (6) by the unorthodox technique of a nonlinear optimization procedure. The advantage of so-doing lies in the determination of the Lagrange multiplier values which, as we have seen, represent the sensitivity of the objective function (i.e. the solution property of most interest) to perturbations in the driving. All constraints are then active, and the solution for the streamfunction is unique, independent of choice of objective function. These are the solutions already referred to and depicted in Figs. 1 and 2.

Although in this fully posed case the value of $\hat{\Psi}$ is uniquely determined, the values of the λ depend upon the choice of F_i. In Figs. 3a–d, we depict contours of constant λ, i.e. regions of equal sensitivity to uncertainty in the driving for four cases:

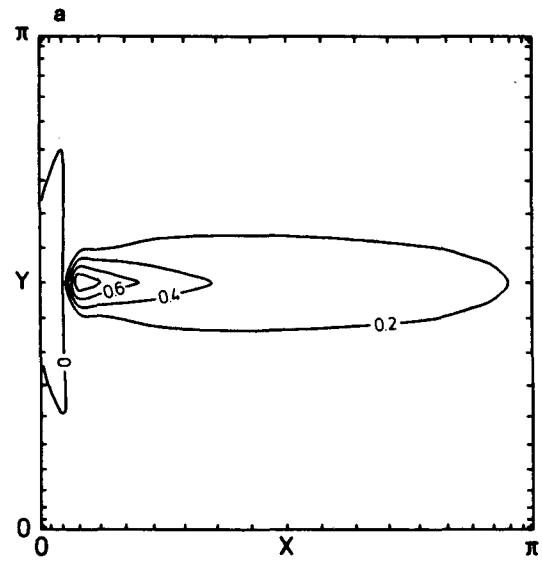

FIG. 3a. Sensitivity of Ψ_{max} of the linear model ($R = 0$) to changes in the bounds of the wind-stress curl. λ is normalized by $\lambda_{max} = 0.08$.

(i) linear (Stommel) model ($R = 0.0$), linear $F_1(\mathbf{X})$ = western boundary current transport.

(ii) linear model ($R = 0.0$), nonlinear $F_2(\mathbf{X}) \propto$ potential energy,

(iii) nonlinear model ($R = 0.01$), linear $F_1(\mathbf{X})$ = western boundary current transport,

(iv) nonlinear model ($R = 0.01$), nonlinear $F_3(\mathbf{X}) \propto$ kinetic energy.

Figure 3a shows how the maximum value of the streamfunction Ψ_{max} is sensitive to changes in the wind-stress curl. The highest sensitivity is at the location Ψ_{max} with a strong fall-off to the north and south, which follows directly from the Sverdrup balance. The fairly rapid decrease of the sensitivity towards the east is due to friction. This result can be understood from the same considerations used by the optimization routine to calculate λ: for each gridpoint separately, the upper (or lower) bound of the forcing is changed marginally while holding all other bounds constant. The corresponding change in the streamfunction leads to a change in the value of $F_1(\mathbf{X})$. From this change, the Lagrange multiplier at the gridpoint is calculated. Because the model is linear, the change of a bound of the forcing can be separated from the fully posed solution by applying a forcing that is zero everywhere except for a delta function like wind-stress curl at one gridpoint. The resulting streamfunction Ψ is sharply peaked at this gridpoint with strong gradients to the north, east and south, while to the west the decrease is small. The local balance is then between the wind-stress curl and bottom friction. The β-effect is comparatively small, provided the delta function is well resolved (i.e. $\Delta x < \epsilon$). Owing to friction, most of the streamlines that extend to the west of the forcing region close off before reaching the western

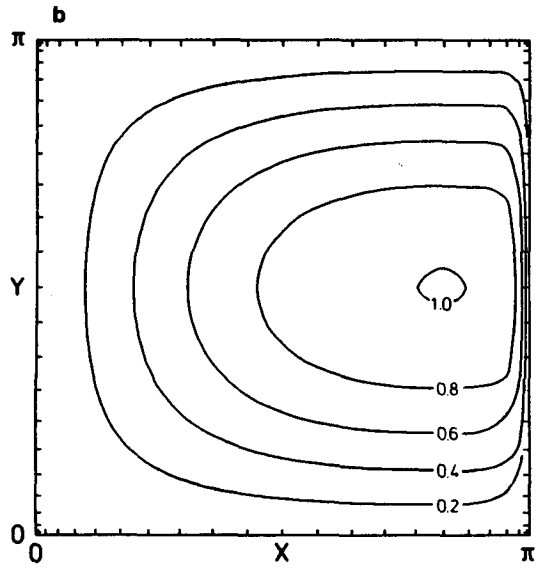

FIG. 3b. Sensitivity λ of the potential energy of the linear model ($R = 0$) to changes in the bounds of the wind-stress curl . λ is normalized by $\lambda_{max} = 0.076$.

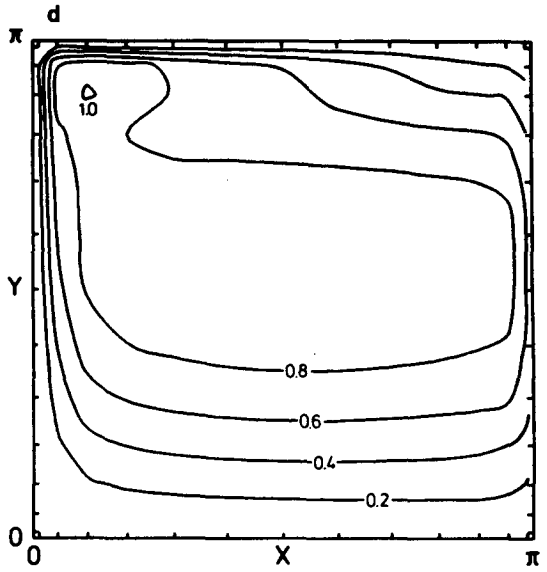

FIG. 3d. As in Fig. 3c but the kinetic energy is used as objective function; $\lambda_{max} = 0.25$.

boundary current. The impact of the delta function forcing on the streamfunction thus decreases to the west, and consequently the *sensitivity* of the value of the streamfunction at any given point on the forcing *decreases to the east* of this point in the corresponding way.

An interesting feature of Fig. 3a is that west of Ψ_{max} there is a region of small negative sensitivity. This means that Ψ_{max} will increase if one decreases the forcing inside this area. The region lies totally inside the western boundary current. A delta functionlike forcing applied at a gridpoint in the boundary current produces a vortex (as it does everywhere in the basin). But here the matching of the streamfunction to the western boundary condition ($\Psi = 0$) cannot be done solely by a frictional boundary current, as there is not enough "room". Note that the width of the western boundary current is determined only by ϵ, while the intensity of the current has no influence on it. Thus, in order to satisfy the boundary condition, Ψ must decrease both at the point of the forcing and locally to the east of it.

In conclusion, if we seek Ψ_{max}, it is most important to measure the wind-stress curl at the location of Ψ_{max} and, to a smaller degree, to the east of it, curl$\underset{\sim}{\tau}$ in the remaining part of the basin being comparatively unimportant.

As this example involves a linear model and a linear objective function, it can also be solved by linear programming methods, such as the Simplex algorithm (Luenberger, 1984; Wunsch, 1984). We have done this calculation and found the solutions of the linear and the nonlinear programming algorithm to be in complete agreement. The Lagrange multipliers are the "dual solution" of linear programming.

In the second example (Fig. 3b), we combine the linear model with a quadratic objective function, the potential energy F_2. The $\hat{\Psi}$ is necessarily the same as in the previous example, but the map of the Lagrange multipliers now depicts instead the sensitivity of the potential energy to changes in the forcing. The sensitivity is strongest where a change in forcing will increase the streamfunction in a large region and where additionally Ψ already has high values. The maximum of λ is thus located near the eastern boundary at $y = \pi/2$. Note the sharp decrease of sensitivity at the eastern wall, a result due to friction. The sensitivity is thus

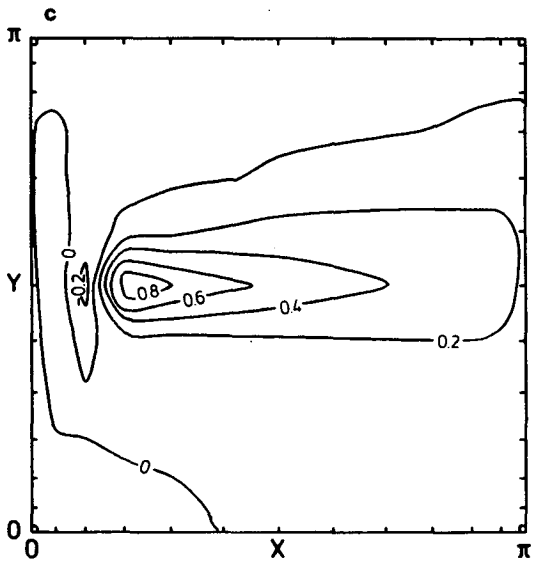

FIG. 3c. As in Fig. 3a but for the nonlinear model ($R = 0.01$); $\lambda_{max} = 0.25$.

nearly a mirror image of the solution itself. This result can be understood in terms of the dominant Sverdrup balance. It is well known that in the Stommel solution, the wind-stress curl directly over the western boundary current has a negligible effect on the flow. But the region of influence of the curl at any point in the interior region extends westward from that point, thus having a greater overall impact on the solution potential energy the further east it is.

We now make the model nonlinear by setting $R = 0.01$ (Fig. 2), and again maximize Ψ_{max}. The effect of the nonlinearity on Ψ_{max} is mainly to move its position eastward as the width of the western boundary current is increased by the inertial effects. A small decrease of the maximum value from 1.85 to 1.80 is also observed. By increasing R, Ψ_{max} will further decrease slowly until the northern boundary current reaches the eastern wall. A further increase of R results in a very strong growth of Ψ_{max} (Veronis, 1966b). The sensitivity of Ψ_{max} to changes in the forcing is mapped in Fig. 3c. The maximum sensitivity has been reduced from 0.08 to 0.05, but the main features are the same as in Fig. 3a. Again the highest sensitivity is at the location of Ψ_{max} with sharp decrease to the north, west and south while to the east the decrease is gentle. The region of negative sensitivity covers the whole northern, and part of the western, boundary current. Values of negative sensitivity, however, are very small, except west of Ψ_{max} where it reaches a value of -0.02 ($\sim$30% of the maximum positive value).

In the fourth example, we combine the nonlinear model with a nonlinear objective function: the kinetic energy integrated over the whole basin. The map of the corresponding Lagrange multipliers is shown in Fig. 3d. The highest sensitivity of the objective function to changes in the forcing is in the recirculation zone in the northwest corner. In the center of the basin values of λ are high with a sharp fall-off at the western and at the eastern boundary while to the north and south the decrease is gentle. The absence of a noticeable increase of the sensitivity to the east is due to the fact that the kinetic energy is located predominantly in the western boundary current and, to a smaller degree, in the northern boundary current. This result explains also why the location of the highest sensitivity is in the north-west. Here an increased forcing acts directly on both the western and the northern boundary current.

It should be clear that the interpretation of the sensitivity maps can be made sensibly in terms of the dynamics—as the flow of information from one part of the system to another. The analysis of the result is not always obvious, depending as it does upon the model parameters, the objective function and the particular region begin perturbed.

b. *Introduction of uncertainty in the forcing*

Consider now the case when upper and lower bounds for the forcing, $\mathbf{U}$ and $\mathbf{L}$, are not identically zero; the optimal solution depends then on the objective function chosen.

To assign values for the bounds on $\text{curl}\tau$, $\mathbf{U}$ and $\mathbf{L}$, assume that we model the subtropical gyre in the North Atlantic. Hellerman and Rosenstein (1983) have estimated the Gulf Stream transport in January (assuming the Sverdrup relation to apply) to be 50 Sv with a standard deviation of 7 Sv. By setting $U_j = 0.15$ and $L_j = -0.15, j = 1, \cdots, 169$, we distribute the uncertainty in $\text{curl}\tau$ homogeneously over the whole basin. The bounding values ± 0.15 correspond to ± 11.8 Sv if we scale the fully posed wind forcing to the mean value of 50 Sv.

The assignment of realistic values to the bounds of the uncertainty of the wind forcing has to be done with great care. As noted above, at the optimal solution, a number of these bounds are binding. The bounds that are not binding do not constrain $F(\mathbf{X})$ and can be omitted from the problem without changing the solution. But for most problems, it is not obvious a priori which constraints will be active at the solution, especially as the addition of new constraints can alter the whole situation.

We will now show results for the fourth problem (iv) above, where now the forcing has been left uncertain to within ± 0.15 at every gridpoint of the model. The solutions that maximize and minimize the objective function are different. Figure 4a depicts the streamfunction that minimizes the kinetic energy E_k. The overall strength of the gyre is much smaller than for the fully posed case, Ψ_{max} has decreased from 1.8 to 1.4 and in the east there is a region of negative Ψ. A small recirculation gyre has separated from the main gyre and the northern boundary current is weak. The E_k is reduced by more than half from 17.3 to 8.2, its smallest possible value for the conditions considered here. The sensitivity of the minimum kinetic energy to changes in the bounds of $\text{curl}\tau$ is mapped in Fig. 4b. The overall resemblance to Fig. 3d is obvious; the main change is in the location of the maximum from the recirculation zone to the center of the basin and the decrease in the maximum absolute value from 0.25 to 0.18. Both changes result directly from the weakened circulation. All λ are negative here; the lower bound L for $\text{curl}\tau$ in (7) has been reached at all grid points.

The solution (Fig. 4c) that maximizes E_k under the same conditions is quite different from the two previous solutions (Fig. 2, Fig. 4a). Here there is a strong northern boundary current, Ψ_{max} has moved to the northwestern corner and has a value of 2.3, and E_k is increased to 32.4, almost double the value of the fully posed solution. It is noticeable that in this model the highest kinetic energy is reached by a strong smooth flow and not by a weaker flow superimposed on a field of strong vortices. The upper bound $\mathbf{U}$ in (7) has been reached everywhere in the basin. Figure 4d depicts the sensitivity of the maximal E_k to changes in the bounds. Compared to the sensitivity for the fully posed solution

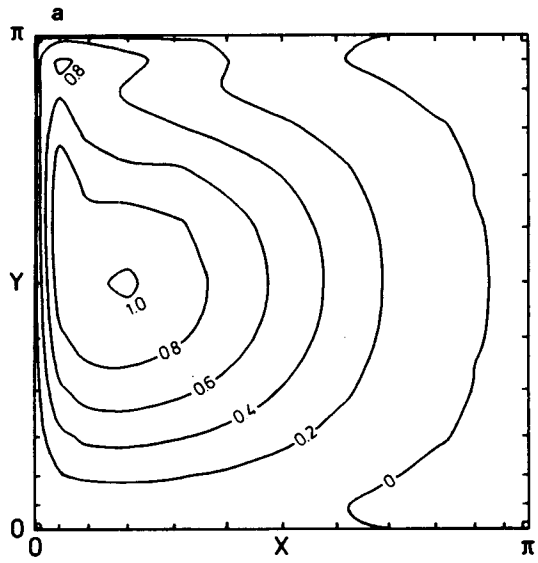

FIG. 4a. Normalized streamfunction Ψ/Ψ_{max} that minimizes the kinetic energy of the nonlinear model ($\epsilon = 0.05$, $R = 0.01$). The forcing, curlτ, has been left uncertain to within ±0.15. $\Psi_{max} = 1.40$, $E_{kin} = 8.22$.

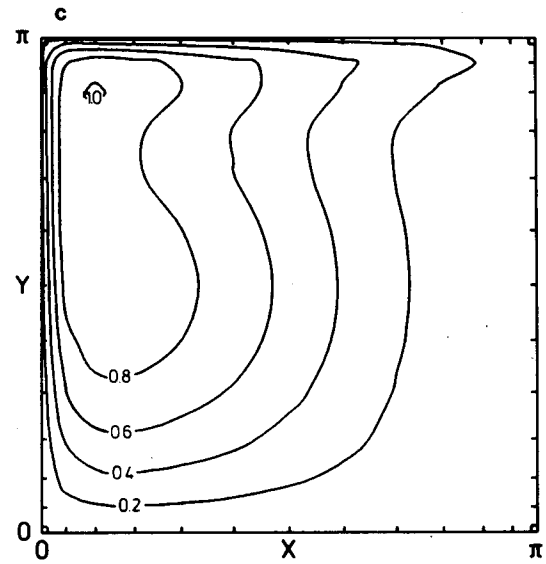

FIG. 4c. As in Fig. 4a but for maximization of the kinetic energy under the same conditions. $\Psi_{max} = 2.28$, $E_{kin} = 32.27$.

(Fig. 3d), the maximum of λ has changed from 0.25 to 0.45. Generally, the sensitivity in the recirculation zone and in the vicinity of the northern boundary current is increased due to the stronger and more nonlinear flow.

The two experiments with uncertain forcing show how the strong nonlinearity of the problem amplifies an uncertainty in the forcing of less than 25% to an uncertainty in the kinetic energy of a factor of 2. The maps of the sensitivity show the location where a reduction in uncertainty of the wind forcing curlτ is most important. If we are interested in the maximum of E_k, we should direct our effort to better estimates of curlτ into the northwestern region of the basin. If, on the other hand, our objective is a good estimate of the minimum of E_k, then we should try to improve our knowledge about curlτ in the center of the basin.

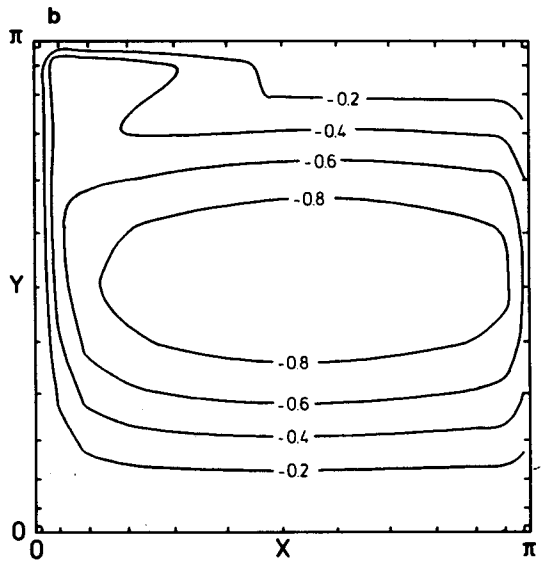

FIG. 4b. Normalized sensitivity $\lambda/|\lambda_{max}|$ of the minimal kinetic energy to changes in the bounds of the uncertainty of the wind-stress curl. This figure corresponds to Fig. 4a. $|\lambda_{max}| = 0.178$.

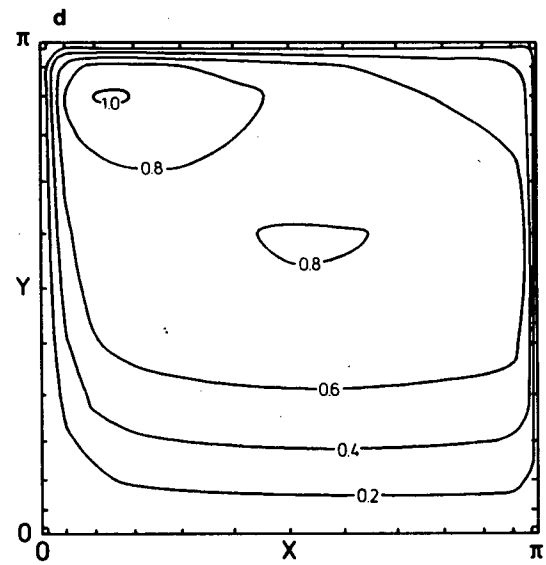

FIG. 4d. As in Fig. 4b but corresponding to maximization of kinetic energy (Fig. 4c). $\lambda_{max} = 0.45$.

c. Combining different kinds of data

The sensitivity analysis depends not only on the objective function but also on the specific combination of constraints with their respective bounds. By adding new data, not only are the values of the Lagrange multipliers altered, but the whole pattern of the sensitivity can change dramatically. Conclusions derived from one example may be only of limited value if new information is added.

Consider now an example combining new data with the nonlinear finite difference circulation model. At the solution, the circulation has to fit every inserted value of the data to within prescribed bounds. We use F_1 as the example. The data that was inserted were described above:

(i) the forcing curlτ over the whole basin,
(ii) the sea surface topography from "altimetry" along a line that runs from west to east and,
(iii) the circulation Γ around a number of intermediate areas inside the basin as measured by acoustic tomography.

Bounds for curlτ are again set to -0.15 and 0.15. For the altimetric constraints, bounds ΔZ correspond to an uncertainty of ± 0.1 m. This uncertainty includes measurement and geoid error as well as the effect of the variability of the ocean circulation. A single altimetric measurement along one track may not achieve such an accuracy, but repetitive measurements can (Wunsch and Zlotnicki, 1984). The question of accuracy can also be posed inversely: how far do we have to increase the accuracy of altimetric measurements until the new data contain significant information? This accuracy depends on the objective function as well as on region of measurement.

The specification of bounds for data derived by tomography is a case that we have tackled inversely. Because the measurement of Γ is hypothetically extraordinarily accurate (Munk and Wunsch, 1982), its bounds are not intended to represent measurement error. Instead they are conceived as describing the uncertainty by which the time averaged or steady state of the general circulation might be represented by limited duration data. A number of different values for the bounds on Γ were tried. For the uncertainties in curlτ, and the topography of ± 0.15 and ± 0.1 m, a value of ± 0.5 for the bounds on the circulation Γ can be regarded as a "threshold" value. For smaller bounds (e.g., ± 0.25) the circulation constraints dominate the solution; all altimetric constraints become inactive. For larger bounds such as ± 1.0 very few circulation constraints are binding, and their influence on the solution is weak.

It remains to choose a latitude for the altimetric track. In the model, surface topography and streamfunction are equivalent, and it is important that the altimetric track does not cross Ψ_{max}. Doing so would put bounds on the value of the objective function which are uninteresting; either those bounds are not reached at the solution or one of the bounds is reached. In the latter case, the value of F_1 is found not by the optimization, but is prescribed by the bound. An infinity of solutions would yield this value of the objective function and the sensitivity analysis is irrelevant.

The altimetric track here runs between the main- and the recirculation gyre and is shown as a solid line in Figs. 5c, 6c. The solution that maximizes Ψ_{max} is shown in Fig. 5. In Fig. 5a, Ψ exhibits a much stronger northern boundary current than in the fully posed case. The maximum has increased from 1.8 to 2.1, but its location is unchanged. Sensitivity of Ψ_{max} to changes in the uncertainty of the forcing is mapped in Fig. 5b. This figure resembles closely the corresponding sensitivity of the fully posed solution (Fig. 3c) but where the maximum value of λ is changed from 0.05 to 0.03. Topographic constraints are binding at four gridpoints in the center of the satellite track. The corresponding sensitivity is shown in Fig. 5c with a maximum of 2×10^{-3}. Compared with the sensitivity of the forcing, this indicates that a reduction of 1 cm in the uncertainty of the topography at the point of highest sensitivity is equally important as a reduction in the uncertainty of curlτ at Ψ_{max} of 6×10^{-4}. Likewise all values of the Lagrange multipliers of the various constraints can be compared.

Constraints derived by "acoustic tomography" are binding in many locations distributed over much of the basin. However, sensitivity is high only in the vicinity of Ψ_{max} (Fig. 5d) with maximal values inside the western boundary current.

In Figs. 5e, f, we display the normalized curlτ which is the new, effective, right-hand side of the dynamical constraints, and its deviation from the initial field of Eq. (5). The optimal solution of Fig. 5a exactly satisfies the dynamical constraints if the curl field of Fig. 5e is substituted on the right-hand side of Eq. (1). In those regions of Fig. 5f where values of $+1$ are found, the new forcing has reached the upper bounds of constraint Eq. (8), and at -1, it has reached the lower bounds.

The example shown here is only one of a large number of problems we have solved with the nonlinear programming algorithm. By changing the locations of the constraints or their corresponding uncertainties the maps of sensitivity can change dramatically, as it can too for a change in objective function. We cannot easily draw conclusions or recommendations of general applicability from specific problems.

d. Uncertainty in a model parameter

In numerical models a number of empirical parameters are used to describe the effect of unresolved processes. The values of these parameters are uncertain to some extent. Often, one needs to understand how this

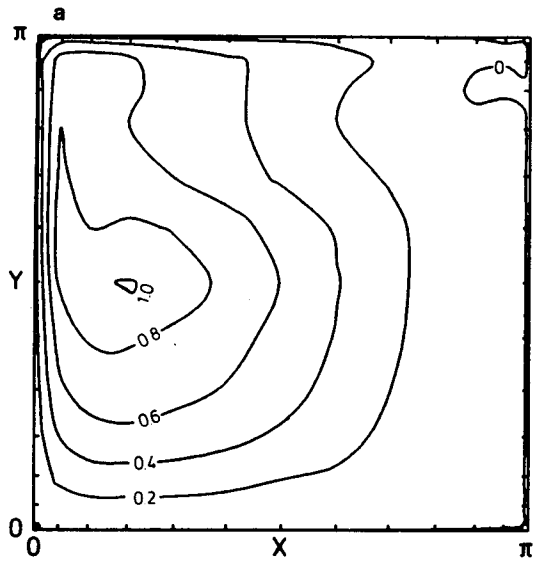

FIG. 5a. Normalized streamfunction Ψ/Ψ_{max} that maximizes the western boundary current transport in the nonlinear model ($\epsilon = 0.05$, $R = 0.01$). The forcing curl$_\tau$ is uncertain to within ± 0.15, the sea-surface topography along the altimetric track (Fig. 5c) is known to within 0.1 m and the circulation Γ is known to within ± 0.5 in the interior of the basin. $\Psi_{max} = 2.12$.

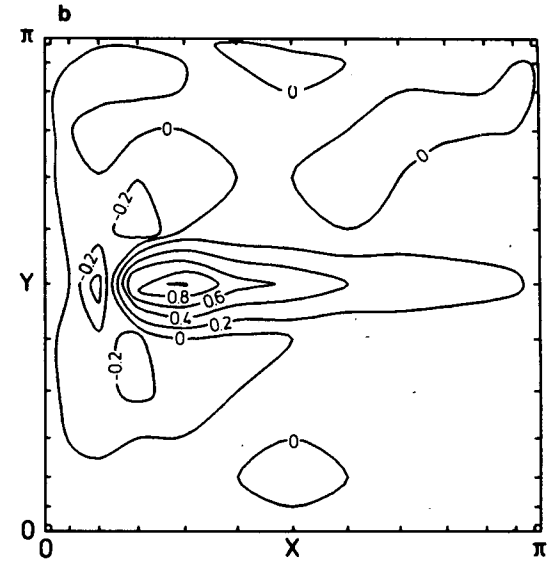

FIG. 5b. Normalized sensitivity λ/λ_{max} of Ψ_{max} to changes in the bounds of the uncertainty of the wind-stress curl. The situation is that of Fig. 5a. $\lambda_{max} = 0.03$.

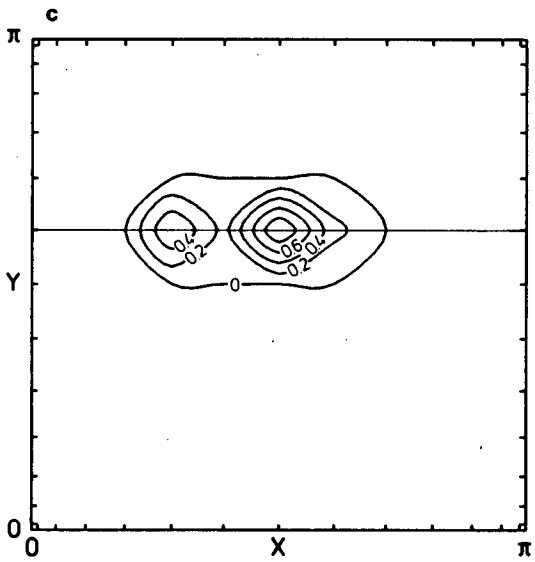

FIG. 5c. Normalized sensitivity λ/λ_{max} of Ψ_{max} to changes in the bound of the uncertainty of the topography along the altimetric track. Track is indicated by a solid line. The situation is that of Fig. 5a. $\lambda_{max} = 0.002$.

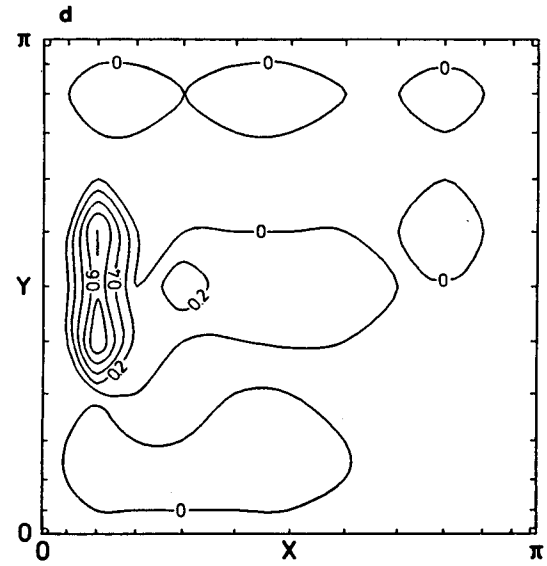

FIG. 5d. Normalized sensitivity λ/λ_{max} of Ψ_{max} to changes in the bound of the uncertainty of the circulation Γ around intermediate areas in the interior of the basin. The location of λ is identified with the center of the corresponding area around which Γ is measured. $\lambda_{max} = 0.011$.

uncertainty translates into uncertainties of the final conclusions.

We will show how the uncertainty of a model parameter in the presence of imperfect data can be incorporated into the solution method. Consider ϵ; it is replaced in the forcing constraints by a variable. The number of variables is increased by one, and the already nonlinear problem becomes even more so.

A reduction of ϵ does not lead directly to an increase in Ψ_{max}. In the linear approximation ($R = 0$), Ψ_{max} is given by the Sverdrup-balance and is independent of friction. In the nonlinear case, however, the situation

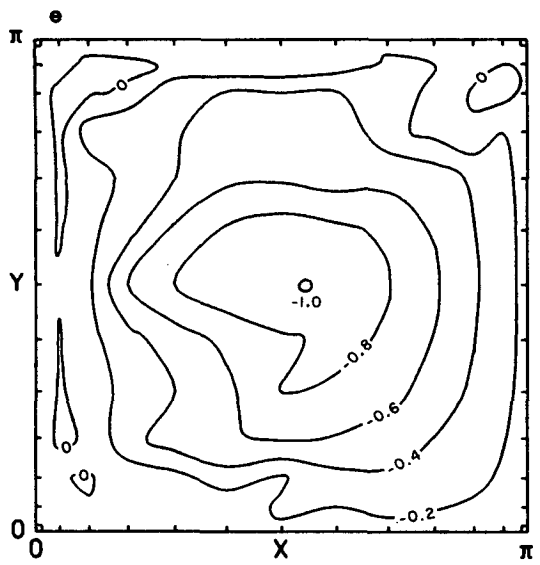

FIG. 5e. The wind-stress curl field which corresponds to the optimal solution shown in Fig. 5a, and which renders the dynamical constraints exactly satisfied. The values have been normalized by division by 1.15, the maximum value.

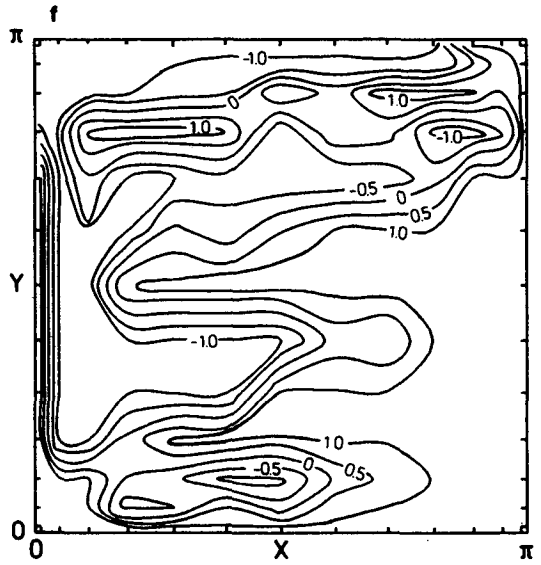

FIG. 5f. Deviation of the optimal forcing field, for the conditions given for Fig. 5a, from the original prescription of the forcing.

changes. As the ratio $\sqrt{R}/\epsilon$ increases past about 2.3, the northern boundary current reaches the eastern wall (Veronis, 1966b). When no additional data beyond the forcing constraints are included, an eastern boundary current will form as $\sqrt{R}/\epsilon$ increases further. Once the northern boundary current reaches the eastern wall the increase in Ψ_{max} is large and rapid. As $\epsilon \to 0$, the increase is unbounded.

When constraints are added however, the situation changes. The solution from the previous example (Fig. 5) is modified as shown in Fig. 6, when the bottom friction is made free. The optimal streamfunction (Fig. 6a) and the sensitivity to changes in the bounds of the forcing (Fig. 6b) are virtually unchanged, but the sensitivity corresponding to the altimetric data (Fig. 6c) is altered. Here only the two easternmost of the previously four binding constraints remain so. The sensitivity of Ψ_{max} to the uncertainty of the data derived by tomography (Fig. 6d) is changed slightly, but the overall pattern of sensitivity to tomographic data remains unchanged.

The reason why the solution for a free bottom-friction parameter is nearly the same as for a fixed ϵ lies in the nonlinearity. Although the change in ϵ is small, the nonlinearity tries to increase the northern boundary current, but is prevented from significant change by the tomographic constraints; these permit only small absolute values of vorticity in the central-northern and north-eastern region of the basin.

If there are no tomographic constraints present, the flow can increase until the eastern boundary current raises the surface topography near the eastern wall by 0.1 m and the altimetric constraints become binding. If, on the other hand, the tomographic constraints are retained and the altimetric constraints are deleted from the system, the solution is again similar to Fig. 6a. The *shape* of Ψ in the interior is highly constrained by the tomographic data. The *level* of Ψ is not controlled by these constraints, but it can be increased only until the resulting increase in nonlinearity of the flow affects the shape of Ψ significantly.

To study in more detail the role of the bottom friction when all three kinds of constraints are present we put bounds on ϵ. This is achieved by adding one more range constraint to the system

$$L_\epsilon \leqslant \epsilon \leqslant U_\epsilon \tag{17}$$

which is treated in the same way as before. By changing the bounds in (17) and solving for the maximum western boundary current transport, we can plot the graph of Ψ_{max} as a function of ϵ (Fig. 6g). The Lagrange multiplier corresponding to (17) describes the slope of the curve. Note the sharp decrease of Ψ_{max} when ϵ becomes smaller than 0.045. In this parameter region the nonlinearity produces an increase in the northern boundary current, which can only be counteracted by an overall decrease in circulation and thus a reduction in Ψ_{max}. Another interesting feature of Fig. 6g is the "jumpy" behavior of Ψ_{max} for increasing ϵ. Although the curve is unimodal (which implies that the problem is well posed), the curve is by no means smooth. The slope changes abruptly when single constraints become binding or nonbinding, making the optimization process difficult.

To find the range of ϵ that is possible in the model and consistent with the driving as specified, the problem

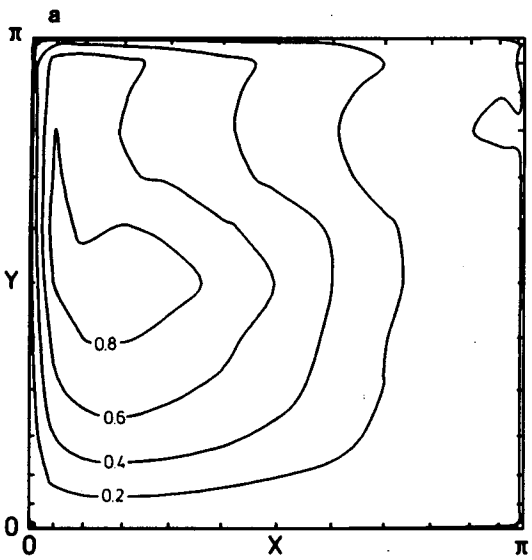

FIG. 6a. As in Fig. 5a but the bottom friction ϵ is treated as a free parameter. Maximum western boundary current transport is obtained for $\epsilon = 0.045$, $\Psi_{max} = 2.13$.

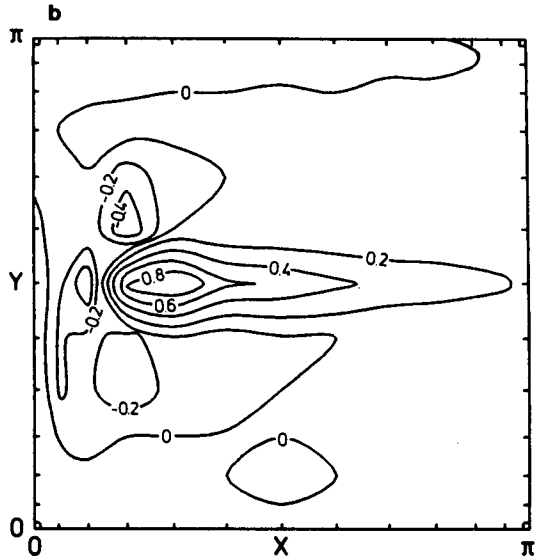

FIG. 6b. As in Fig. 5b but for free bottom friction. $\lambda_{max} = 0.03$.

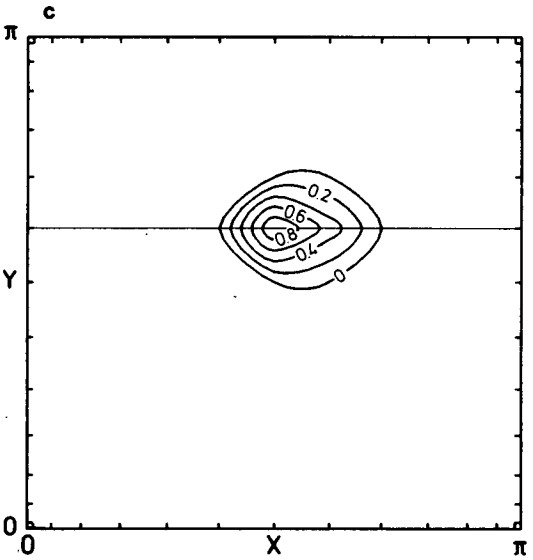

FIG. 6c. As in Fig. 5c but for free bottom friction. $\lambda_{max} = 0.002$.

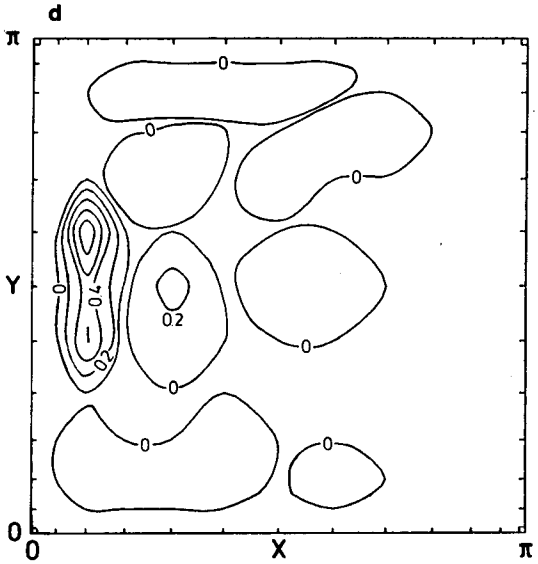

FIG. 6d. As in Fig. 5d but for free bottom friction. $\lambda_{max} = 0.015$.

was solved with ϵ used as the objective function. The result was $0.03 \leqslant \epsilon \leqslant 0.07$. Thus the value is determined from the dynamical and data constraints to within a factor of 1.5 of the correct value (0.05).

5. The two-layer model

a. Description of the model

The model used to this point has been a special one, both barotropic and steady. A virtue is that it has been well studied by more conventional solution methods and which has permitted us to focus more precisely upon the optimization, or inverse, procedures rather than the model itself. To show that optimization/inverse methods are applicable to more interesting models, and to study the impact of adding yet another data type, we will now turn to a two-layer model. Again the flow is described by the time independent vorticity equations which have been vertically integrated over the depth of each layer. The equations have been made nondimensional as above:

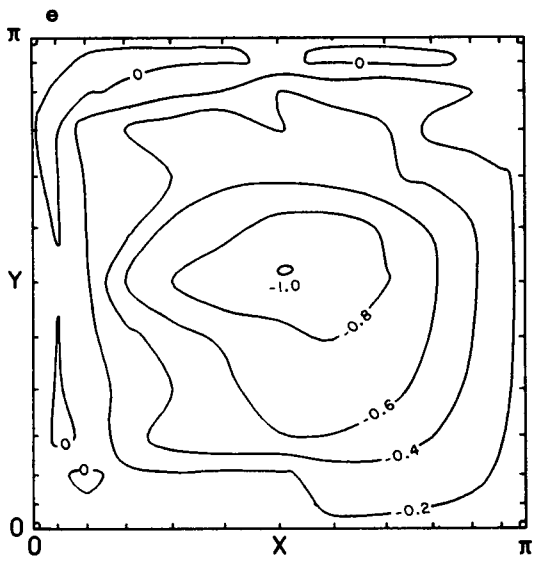

FIG. 6e. As in Fig. 5e but showing the normalized wind curl which corresponds to the solution of Fig. 6a, with free bottom friction.

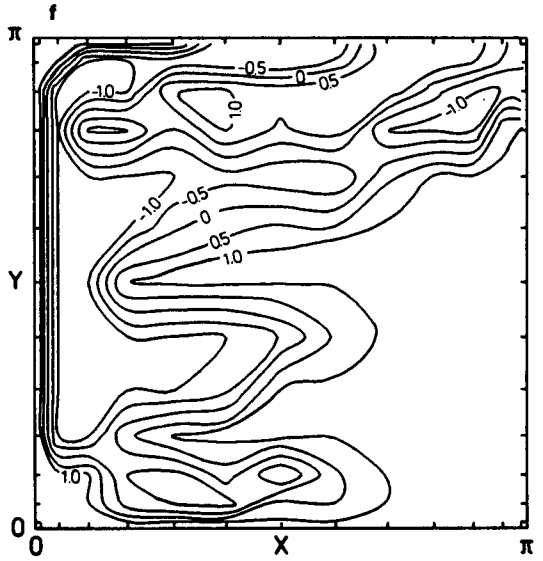

FIG. 6f. As in Fig. 5f but the normalized deviation of curl field of Fig. 6e from the initial field.

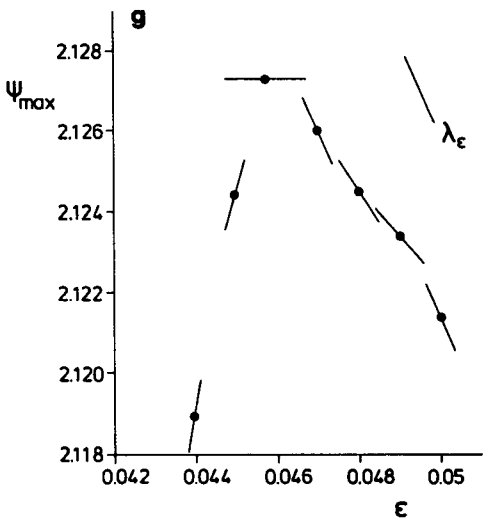

FIG. 6g. Maximum western boundary current transport Ψ_{max} as a function of bottom friction parameter ϵ. Uncertainty in the forcing curlτ and in the inserted topographic and tomographic data is the same as in Figs. 5a–5d. Straight lines indicate the slope of the function as calculated by the sensitivity analysis.

$$RJ(\Psi_1, \nabla^2\Psi_1) + \frac{\partial \Psi_1}{\partial x} + H_1 J(\Psi_1, \Psi_2 - \Psi_1) + H_1\epsilon_1(\nabla^2\Psi_1 - \nabla^2\Psi_2) - \text{curl}_\tau = 0 \quad (18a)$$

$$RJ(\Psi_2, \nabla^2\Psi_2) + \frac{\partial \Psi_2}{\partial x} + H_2 J(\Psi_2, \Psi_1 - \Psi_2) + H_2\epsilon_1(\nabla^2\Psi_2 - \nabla^2\Psi_1) - H_2\epsilon_2\nabla^2\Psi_2 = 0. \quad (18b)$$

Indices 1 and 2 refer to upper and lower layer respectively. The H_1 and H_2 are the relative depth of the two layers, which communicate by interfacial friction and by vortex-stretching produced by deformation of the interface between the two layers. The ϵ_1 is the interfacial friction coefficient and ϵ_2 is for the bottom friction. Boundary conditions are $\Psi_1 = \Psi_2 = 0$ at $x = 0, \pi$ and $y = 0, \pi$.

The same model has been used by many authors (e.g., Ierley and Young, 1983) to study the homogenization of potential vorticity either by adding time and using an eddy-resolving discretization, or by the addition of a diffusion term for potential vorticity. Here we study a circulation that resembles somewhat the single layer solution discussed in the previous section. The forcing, curlτ, is unchanged, and the nondimensional parameters are

$$\epsilon_1 = \epsilon_2 = 0.4$$

$$R = 0.05$$

$$H_1 = H_2 = 0.5.$$

The model grid consists of 11×11 points in each layer and is stretched for better resolution near the boundaries. The fully posed solution as determined from the same active set algorithm is shown in Figs. 7a to 7d. The barotropic streamfunction $\Psi_B = \Psi_1 + \Psi_2$ (Fig. 7d) exhibits a northern boundary current that does not extend to the eastern boundary. The main difference from the single layer case is that recirculation and main gyres have merged and that the maximum of the barotropic streamfunction has moved to the northwest corner.

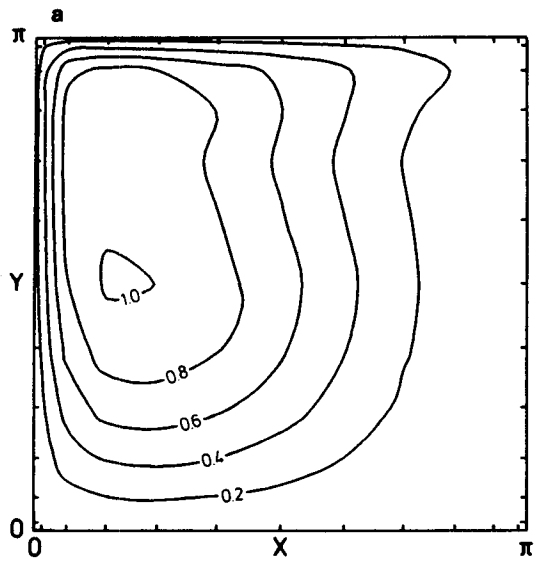

FIG. 7a. Normalized streamfunction $\Psi_1/\Psi_{1,\max}$ for the upper layer of the two layer model. Nondimensional parameters are given in the text. The forcing curlτ is known perfectly. $\Psi_{1,\max} = 1.36$.

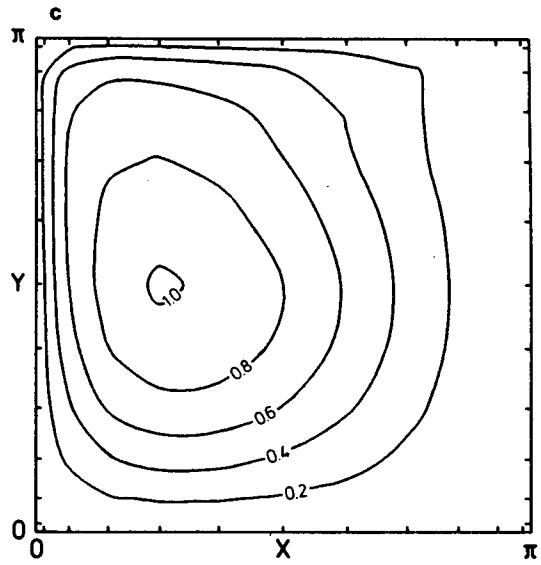

FIG. 7c. Temperature field $\Psi_1 - \Psi_2$ normalized by its maximum value corresponding to Figs. 7a and 7b. $(\Psi_1 - \Psi_2)_{\max} = 0.99$.

Temperature in this model is conventionally identified as $\Psi_1 - \Psi_2$. The interface roughly represents the main thermocline, being bowl-shaped with the deepest part near the western boundary (Fig. 7c).

The flow in the upper layer (Fig. 7a) is stronger than in the lower layer (Fig. 7b). The maximum of the streamfunction Ψ_1 is in the center of the main, wind-driven gyre, while in the lower layer the whole flow is shifted more to the northwest. For Ψ_2 the nonlinearity is much more prominent than for Ψ_1.

b. *Insertion of temperature data*

Uncertainty in the forcing is introduced by again prescribing bounds for curlτ; values for these bounds are the same as in the single layer case. Temperature data are simulated by taking $\Psi_1 - \Psi_2$ of the fully posed solution. The corresponding constraints are written

$$L_j \leq [(\Psi_1 - \Psi_2) - (\Psi_1 - \Psi_2)_{\text{fully posed}}] \leq U_j, \quad j = 122, \cdots, 242 \quad (19)$$

where all streamfunction values are taken at the same

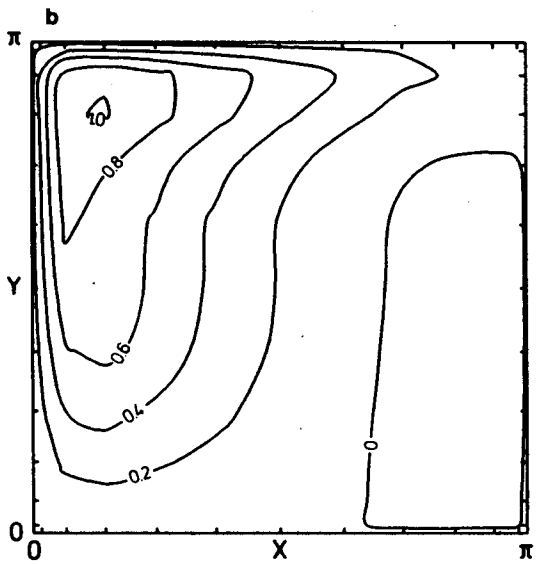

FIG. 7b. As in Fig. 7a but for lower layer. $\Psi_{2,\max} = 0.66$.

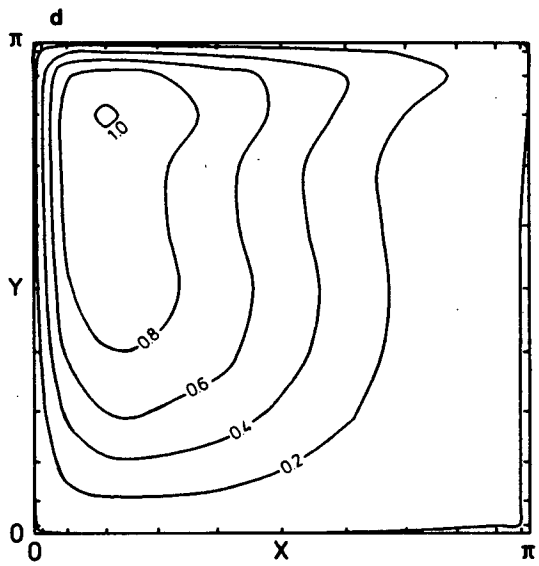

FIG. 7d. As in Fig. 7a but for the barotropic streamfunction $\Psi_B = \Psi_1 + \Psi_2$. $\Psi_{B,\max} = 2.02$.

gridpoint. Bounds for temperature are again meant to describe the uncertainty of a point measurement as representative of the mean. Values for the bounds were derived from threshold values such that some temperature constraints become active while others do not. The values are $L_j = -0.2$ and $U_j = 0.2$, $j = 122, \cdots, 242$. The temperature constraints (19) are added to the forcing constraints of the upper layer and the dynamical constraints of the lower layer leading to a system equivalent to Eq. (11). No slackness is introduced into the equation for the lower layer. This equation does not involve any measured quantity and we postulate that the dynamics are described adequately by Eq. (18b). Upper and lower bounds for this equation are identically zero and are thus equality constraints.

The solution that maximizes the maximum of Ψ_B is shown in Figs. 8a to 8h. The barotropic streamfunction (Fig. 8d) has a maximum value of 2.7, an increase of about 30% relative to the fully posed case (Fig. 7d). In each of the layers the northern boundary current reaches the eastern wall (Fig. 8a, 8b), but no eastern boundary current is observed. The shape of the temperature field $\Psi_1 - \Psi_2$ (Fig. 8c) remains practically unchanged while its amplitude has increased from 1.0 to 1.2. The difference between the two temperature fields (Figs. 8c and 7c) is depicted in Fig. 8g. This difference field is bounded to ± 0.2 by the temperature constraints. Near the walls the temperature difference is small, as a result of the boundary condition for Ψ_1 and Ψ_2. Temperature bounds are reached in the northern and northwestern region. Here the sensitivity of the objective function to changes in the bounds is nonzero. As can be seen in Fig. 8f, the sensitivity is highest to the east of the location of the maximum of Ψ_B. Note that at the location of $\psi_{B,\max}$, the sensitivity is zero as the temperature bounds are not reached.

The sensitivity of $\Psi_{B,\max}$ to changes in the bounds of the forcing is shown in Fig. 8e. We observe a sharply peaked local maximum of λ at the location of $\Psi_{B,\max}$ while in most of the basin the sensitivity is nearly zero. Regions of small negative sensitivity are in the southwest and between $\Psi_{B,\max}$ and the western and northern boundaries.

The Lagrange multipliers for the lower layer dynamical constraints are mapped in Fig. 8f and describe the sensitivity of the maximum of Ψ_B to hypothetical violations in Eq. (18b) if, for example, some physics was missing or improperly imposed (e.g, the value of ϵ_2).

We have shown that temperature information can be inserted into finite-difference models like any other information through the optimization method. For the specific example shown here, uncertainty in the forcing is only locally important, but the uncertainty of the temperature is important over a much larger area. This latter area increases if we reduce the bounds for the temperature constraints.

6. Conclusions and outlook

When studying the oceanic circulation with models, a serious question arises: How accurate are the conclusions that we can derive from the model when we insert more or less reliable measured data? The method used here calculates bounds of uncertainty for all quantities of interest. The calculation must be done separately for each bound of each individual quantity (objective function). We cannot find bounds for different objective functions simultaneously.

A major result of the algorithm is that we calculate the quantitative sensitivity of our objective function to change in the data or its uncertainty. We can map this sensitivity and observe how it is altered by the addition of measured, or hypothetical data. Thus the method can be applied to the study of different observational strategies.

The very general form of the constrained problem [Eq. (9)] means that the use of models with additional layers, more complex physics and time dependence is not a matter of principle but rather one of computer speed and storage, and efficiency of the solution algorithms. In many ways, our understanding of how best to solve a given model is at a primitive stage (we are unaware of previous attempts to apply nonlinear optimization methods to an oceanic GCM) and much further experience will be needed.

The method employed here contrasts with more conventional ones, usually related closely to least-squares, in that it is underdetermined by the constraints. In all our solutions, there is a forcing field for which the streamfunction exactly satisfies the dynamical constraints (see Figs. 5f, 6f). This constraint satisfaction is not characteristic of the variational approaches of Wahba and Wendelburger (1980) and others described previously. There the systems are intrinsically infeasible (i.e. overdetermined), and there is a competition between the demands of the data and of the dynamics. One should not over-emphasize the differences between schemes which are formally overdetermined and formally underdetermined, as it is well-known in inverse theory and elsewhere that the distinction is often almost purely semantic (e.g. Wunsch, 1985).

In working with real, rather than artificial, data one must anticipate that when initially posed, the combination of dynamical and data constraints will show contradictions (called "infeasibility"). Such situations usually call for a two-step review. The first stage is a reexamination of whether the data bounds are truly realistic. If this review leaves the infeasibility unresolved, one is driven to reexamine and probably modify the model itself. These modifications can range from simple parameter changes, as in our example of finding the range of friction parameters consistent with the

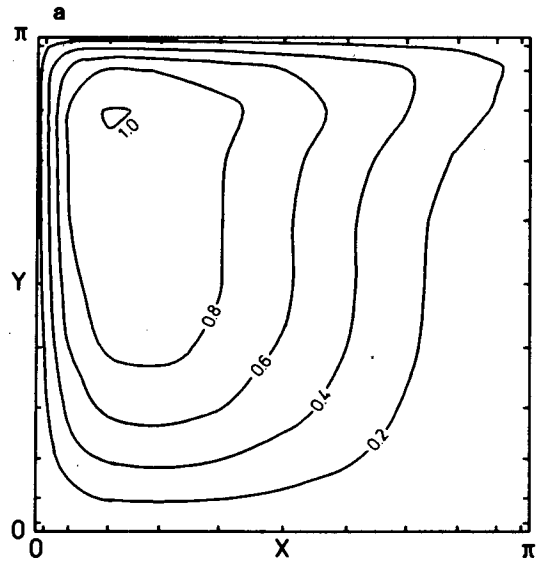

FIG. 8a. Normalized streamfunction $\Psi_1/\Psi_{1,\max}$ of the upper layer that maximizes the western boundary current transport $\Psi_{B,\max}$. The forcing curlτ is uncertain to within 0.15 and the temperature $\Psi_1 - \Psi_2$ is known to within 0.2. $\Psi_{1,\max} = 1.779$.

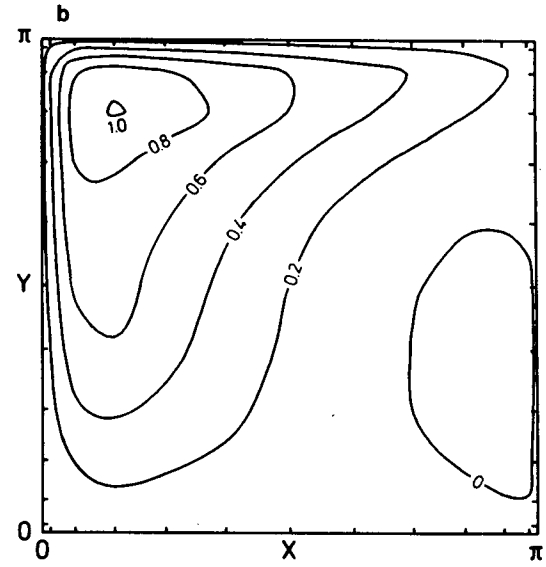

FIG. 8b. As in 8a but for lower layer. $\Psi_{2,\max} = 0.88$.

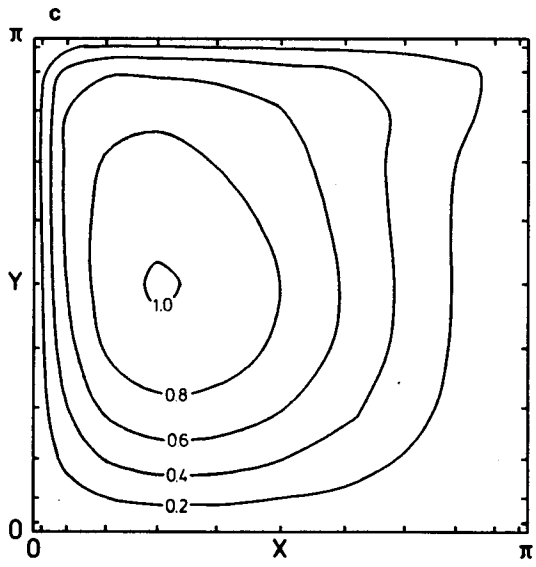

FIG. 8c. Normalized temperature field $\Psi_1 - \Psi_2$, corresponding to Figs. 8a and 8b. $(\Psi_1 - \Psi_2)_{\max} = 1.19$.

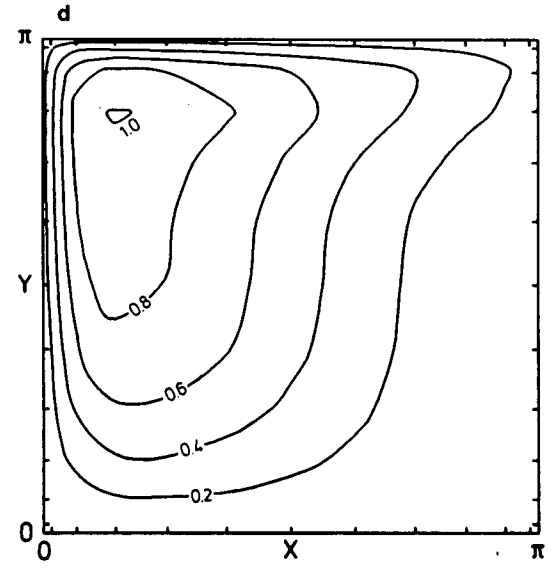

FIG. 8d. As in 8a but for barotropic streamfunction Ψ_B. $\Psi_{B,\max} = 2.66$.

constraints to, if necessary, major changes such as the addition of more layers, or entirely new physics to the model.

Somewhat paradoxically, unresolvable infeasibilities are desirable. When a model is clearly inconsistent with observations, one has demonstrated the need for a more complex, or even entirely different model. These demonstrations are how the science progresses.

The optimization method is currently being used in conjunction with a realistic general circulation model. As the number of computations increases with the number of unknowns cubed, we are beginning with a small number of variables that describe, for example, the amplitudes of the empirical orthogonal functions of the windstress. From these, the circulation model will calculate several thousand values for currents,

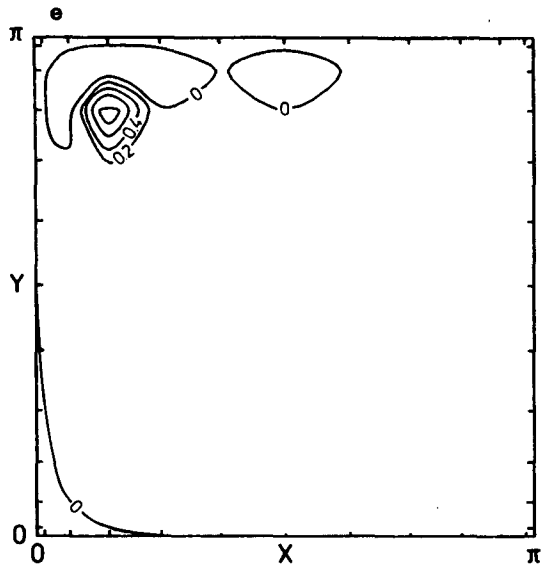

FIG. 8e. Normalized sensitivity λ/λ_{max} of the maximum western boundary current transport to changes in the bounds of the uncertainty of $\text{curl}\tau$. $\lambda_{max} = 0.001$.

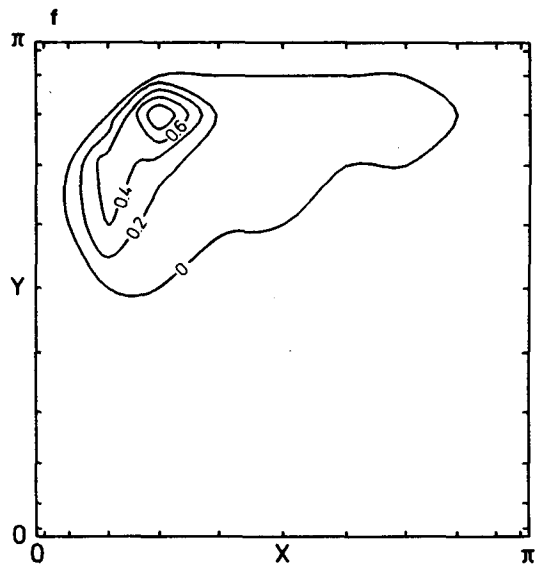

FIG. 8f. Normalized sensitivity λ/λ_{max} of the maximum western boundary current transport to changes in the bounds of the temperature $\Psi_1 - \Psi_2$. $\lambda_{max} = 0.001$.

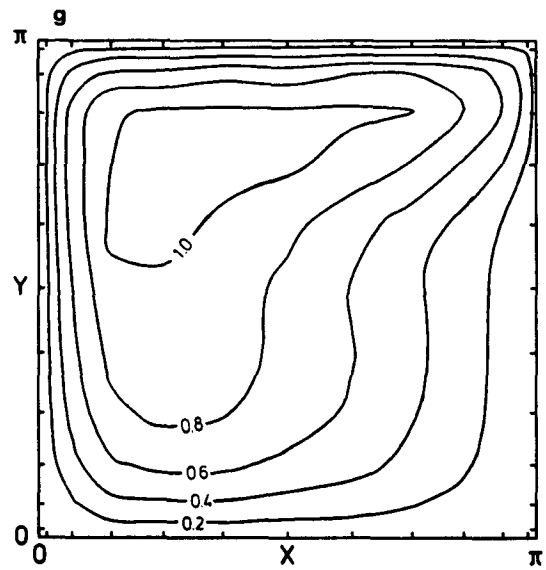

FIG. 8g. Deviation of the temperature $\Psi_1 - \Psi_2$ of the solution that maximizes the western boundary current transport $\Psi_{B,max}$ from the temperature of the fully posed solution. The contourplot is normalized to 0.2, the highest possible deviation according to the temperature constraints.

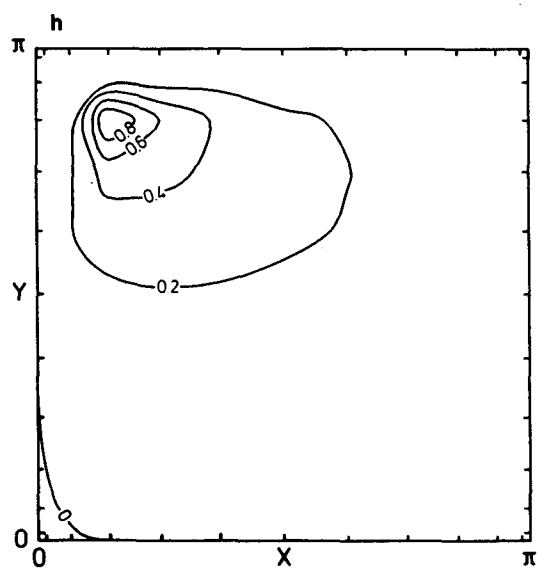

FIG. 8h. Normalized sensitivity λ/λ_{max} of the maximum western boundary current transport to violations of the dynamics (Eq. 18b) of the lower layer, such as erroneous bottom friction parameterization. $\lambda_{max} = 0.001$.

temperature, salinity, etc., which in turn are used to calculate an objective function such as surface temperature gradient or meridional heat transport.

Acknowledgments. This work was supported in part by the National Science Foundation under Grant OCE 80-185140, and by the National Aeronautics and Space Administration under Grants NAG 6-9 and NAG 5-534. JS was supported in part by the Bundesministerium für Forschung und Technologie on his return to Hamburg. The computations were performed at the computing centers of MIT and the Goddard Space Flight Center. We are grateful to Barbara Grant and Charmaine King for computing assistance.

APPENDIX

Experience with the Minimization Procedure

Provided $F(\mathbf{X})$ is convex, the algorithm used will converge to the solution $\hat{\mathbf{X}}$ in a mathematical sense, that is, ultimately, regardless of initial choice of the starting point $\mathbf{X}_0$ and the initial penalty parameter δ_0 and regardless of the scaling. But, numerically, there are problems. Computation time can become excessive and inhibit convergence, or the algorithm can diverge (especially for large δ) owing to a lack of computational accuracy and amplification of roundoff errors.

Our experience with this model is that the choice of the starting point $\mathbf{X}_0$ is not critical, but the initial penalty parameter δ_0 must be chosen with care. If the initial δ_0 is too small, the vector $\mathbf{X}$ that minimizes $L(\mathbf{X}, \lambda, \delta)$ is situated very far away from the feasible region. Here δ has to be augmented several times until feasibility is obtained with lots of useless calculations made. If, on the other hand, the initial δ_0 chosen is too large, too much weight is put on feasibility and not enough care is taken to minimize $F(\mathbf{X})$. It may happen in this case, and it frequently does, that δ is augmented again and again, leading to even smaller $\mathbf{C}_r$, where $\mathbf{C}_r$ is the residual value of C in the minimum of L. The minimum of $F(X)$, however, is not found in this case since small changes in $\mathbf{X}$, that result in small changes in $F(\mathbf{X})$ will cause very large changes in $\mathbf{C}_r$. The method does not converge to the correct solution $\hat{\mathbf{X}}$ because of insufficient accuracy during the line search. This accuracy can be chosen as an input parameter of the minimization routine. Generally, there is a trade-off between the number of iterations to be performed and the accuracy of the line search.

The scaling of $\mathbf{C}(\mathbf{X})$ is also of great importance as it impacts, via the Lagrange multipliers, on the "active set" strategy.

Although accurate linear minimization of $L(\mathbf{X}, \lambda, \delta)$ along the line of search will generally reduce the number of iterations, this usually results in an increase in the number of evaluations of $L(\mathbf{X}, \lambda, \delta)$ required for each iteration. As a general rule, the literature suggests that it is usually more efficient to perform a low accuracy linear minimization. But for our purposes, we found the opposite to be true. One reason for this difference may be that the rank of the matrix that has to be inverted here for each iteration is of the order of several hundred, unlike more conventional applications.

All weighted constraints are multiplied by scaling factors W_f for forcing, W_a for altimetric and W_t for tomographic constraints. The W are chosen such that all nonzero derivatives $\partial C_j/\partial X_i$ lie in the interval [0.1, 10]. Because the Lagrange multipliers are inversely proportional to the weight, W, they have been rescaled by multiplication by W once the optimal solution has been calculated.

A feeling for the computing resources required to solve problems using this algorithm may be obtained by noting that the solution for the one-layer model shown in Fig. 5 required approximately 15 minutes on a Cyber 205 with a purely scalar code. There are more than 500 variables involved in the calculations (physical plus slack variables), and a substantial amount of virtual storage was required, with much of the time involved purely in page swapping. No attempt has yet been made by us to take advantage of the sparse nature of the defining matrices, nor to vectorize the problem.

REFERENCES

Bennett, A. F., and P. C. McIntosh, 1982: Open ocean modeling as an inverse problem: tidal theory. *J. Phys. Oceanogr.*, **12,** 1004–1018.

Gill, P. E., and W. Murray, 1972: Quasi-Newton methods for unconstrained optimization. *J. Inst. Math. Its Appl.*, **9,** 91–108.

Harrison, D. E., and S. Stalos, 1982: On the wind-driven ocean circulation. *J. Mar. Res.*, **40,** 773–791.

Hellerman, S., and M. Rosenstein, 1983: Normal monthly wind stress over the world ocean with error estimates. *J. Phys. Oceanogr.*, **13,** 1093–1104.

Ierley, G. R., and W. R. Young, 1983: Can the western boundary layer affect the potential vorticity distribution in the Sverdrup interior of a wind gyre? *J. Phys. Oceanogr.*, **13,** 1753–1763.

Luenberger, D. C., 1984: *Linear and Nonlinear Programming,* Addison-Wesley, 491 pp.

Malanotte-Rizzoli, P., and W. R. Holland, 1986: Data constraints applied to models of the ocean circulation. Part 1. The steady case. *J. Phys. Oceanogr.*, **43,** 1665–1682.

Munk, W., and C. Wunsch, 1982: Observing the ocean in the 1990's. *Phil. Trans. Roy. Soc. London,* **A307,** 439–464.

Numerical Algorithms Group, 1984: *Fortran Library Manual, Mark II.,* 6 vols.

Roache, P. J., 1982: *Computational Fluid Dynamics.* Hermosa, 446 pp.

Sasaki, Y., 1958: An objective analysis based on the variational method. *J. Meteor. Soc. Japan,* **36,** 1–12.

Schröter, J., 1984: An optimization approach to a finite difference ocean circulation model, Ocean Modelling 55, 4-7. Unpublished manuscript.

Stommel, H., 1948: The westward intensification of wind-driven ocean currents. *Trans. Amer. Geophys. Union,* **29,** 202–206.

Veronis, G., 1966a: Wind-driven ocean circulation—Part 1. Linear theory and perturbation analysis. *Deep-Sea Res.*, **13,** 17–29.

——, 1966b: Wind-driven ocean circulation—Part 2. Numerical solutions of the non-linear problem. *Deep-Sea Res.*, **13,** 31–55.

Wahba, G., and J. Wendelberger, 1980: New mathematical methods for variational objective analysis using splines and cross validation. *Mon. Wea. Rev.*, **108,** 1122–1143.

Wunsch, C., 1984: An eclectic Atlantic Ocean circulation model. Part 1: The meridional flux of heat. *J. Phys. Oceanogr.*, **14,** 1712–1733.

——, 1985: Can a tracer field be inverted for velocity? *J. Phys. Oceanogr.*, **15,** 1521–1531.

——, and V. Zlotnicki, 1984: The accuracy of altimetric surfaces. *Geophys. J. Roy. Astron. Soc.*, **78,** 795–808.